Research Article

N and Fe doped NiO nanoparticles for enhanced photocatalytic degradation of azo dye methylene blue in the presence of visible light

Martha Ramesh[1] (ID)

Abstract

Pure NiO, N-doped, Fe-doped, N and Fe codoped NiO NPs were fabricated via a precipitation process. The powder X-ray diffraction (XRD) revealed the face centered cubic phase of NiO products. The full width at half maximum (FWHM) of the XRD peak was steadily enlarged with the order of elements N, Fe, N/Fe doped to NiO, and shifted towards a greater angle due to decrease in grain size, as shown by XRD. The average crystallite size of NiO products was calculated, ranging from 6.67 to 3.76 nm, according to the Debye Scherrer formula. The scanning electron microscopy (SEM) demonstrated considerable morphological changes in the produced nanoparticles, including those directed to rock-like geometries (NiO and Fe/NiO nanoparticles) while gas covered-nanocrystals (N/NiO and N/Fe/NiO nanoparticles) were formed using precipitation method. The particle size range of 10–50 nm was estimated using the bar scale in transmission electron microscopy (TEM) pictures. The elemental composition of Ni, O, Fe and N atoms in the respected samples was analyzed by Energy Dispersive X-Ray Analysis (EDX). Photoluminescence (PL) showed band edge emission at 370 nm. The band edge-absorption peak, which is caused by electronic transitions between energy levels, is determined to be in the range 314–325 nm. A UV–Vis analysis found an energy gap amid 3.2 eV and 2.5 eV. The chemical condition of the Fe and N doped NiO composites were validated using XPS. Using visible photo application of undoped and doped NiO NPs, the degradation of an azo dye termed methylene blue was examined. It was N/Fe/NiO (79.8%), Fe/NiO (76%), N/NiO (73%), and NiO (62%) throughout the 6 h irradiation duration. Increased production of $OH^{\cdot}$ radicals was detected in fluorescence tests using terephthalic acid (TA) for N/Fe/NiO NPs, indicating the higher photo-degradation described. Furthermore, the degradation trends of both undoped and doped NiO NPs closely matched the pseudo first order kinetics, according to the kinetic analysis. There was also a suggestion for a thorough MB breakdown mechanism.

Keywords Dopant · Polluted water · Degradation · Optical properties · Photo-catalysis

1 Introduction

Azo dye like methylene blue (MB) is extensively used in fabric industry, but contaminant of serious concern for their toxicological properties and widespread presence in textile water [1, 2]. To extract dye from effluent, physical, biological and chemical treatments were developed [3–6].

Photocatalysis is better alternative since it can mineralize pollutants completely without producing harmful by-products [7]. In this regard, certain materials could be employed as photocatalyst to accelerate the photoreaction. For example, Subash and co-workers discovered that hydrothermal produced Nb_2O_5 nanoparticles could break down MB photo catalytically. According to these reports, a maximum decolorization of 90% was reported for a low

initial dye concentration of 10 mg/L [8]. Fe_2O_3 nanoparticles have been widely used as a heterogeneous photocatalyst in recent decades. Nevertheless, its poor electrical conductivity, poor adsorption yields high rate of charge carrier recombination. In addition, the hydrophobic surface of Fe_2O_3 can result in hydrophobic interactions between particles, which will promote particle agglomeration and lower surface area, limiting it to be an ideal photo-catalyst [9]. TiO_2 and MnO_2 were renowned nanomaterials for their enormous surface area and high photo efficiency. But, they have a huge band gap (4–6 eV), which means it can only absorb UV light, is a substantial hurdle to its real-world use [10, 11]. Recently, Subash D et al. [12] synthesized Bi_2O_3 nano layers by chemical deposition route. Photocatalytic degradation of organic dyes revealed that Bi_2O_3 has lower photosensitivity and creates fewer pairs of electrons and holes, restricting their ability to use the entire UV spectrum. Although the addition of lanthanum metal (La) increases the photocatalytic efficiency of Bi_2O_3, it is not widely available due to the laborious, time-consuming, and expensive mining procedure. Therefore, for the purpose of photo-catalysis, a more photosensitive material is desirable.

NiO can be used as an alternative material due to their abundance, high adsorptive affinity, high photosensitivity and low band gap [13]. Recently, NiO was produced via a simple chemical process, showed noticeable visible light activity on the degradation of MB. At pH 2, the level of breakdown of MB was discovered to be 98.7%. The findings suggest that the NiO NPs have good photocatalytic activity for removing MB dye from their aqueous solution [14]. However, under normal reaction conditions, its practical applicability is limited. In this scenario, transition metal substitution doping (Mn, Cu, Fe, etc.) for NiO is considered. Notably, Eliza et al. [15] documented that the improved photo efficiency of the Fe/ZnO compound, iron (Fe) ions incorporation is expected to minimize charge recombination, resulting in a longer charge diffusion extent and improved photocatalytic activity. While Fe doping lower the energy gap, it would be difficult to incorporate it into the O ($\sim R_{Fe} > R_O$) site of NiO crystal, as witnessed by the much higher formation energy needed for Fe substitution. Therefore, replacing with non-metal, nitrogen (N) doped NiO is another promising methodology [16].

Though there are several methods like thermal decomposition [17], sol gel [18], chemical [19], hydrothermal [20], anodic plasma [21], sonochemical [22], solvothermal [23], and microemulsion [24] for developing of NiO nanostructures, chemical precipitation is widely researched. It allows for low-temperature production, superior homogeneity and purity, high yield, and cost effectiveness.

This paper focused on the preparation of N and Fe doped NiO nanocomposites. The influence of doping on the visible light absorption and associating property enhancements, as well as their impacts on MB photo deterioration were investigated. The insertion of Fe^{3+} or N^{3-} into the matrix of NiO replaces some Ni^{3+} ions, and creates abundant doping energy levels as well as charge compensating cation vacancies in the NiO lattice points, improving electrostatic attraction between opposite charged ions, which can affect the adsorption mechanism. Doping ions may cause NiO to shrink in size, allowing charge carriers to travel to the reaction sites on the surface and minimizing recombination. For N/Fe/NiO, the intensity of the PL spectra reduced, which corresponded to a decrease in photo-generated pairs and a decrease in electron–hole recombination, which increased photocatalytic activity.

2 Materials and methods

2.1 Materials

Sigma Aldrich provided the nickel nitrate hexahydrate ($6H_2O. Ni(NO_3)_2$), urea ($CO(NH_2)_2$), sodium hydroxide (NaOH), sodium dodecyl sulphate (SDS), and methyl blue and iron (III) nitrate nonahydrate ($9H_2O. Fe(NO_3)$).

2.2 Synthesis of NiO nanoparticles and its nanocomposites

In a standard synthesis, 2.76 g of $6H_2O.Ni(NO_3)_2$ and 30 mg of SDS were dissolved in a 100 mL deionised water, and then 0.1 M of NaOH was slowly applied to the above solution while vigorously agitated for 2 h at ambient conditions. The final mixture was washed before being heated for 12 h at 80 °C in a vacuum. The NiO NPs were produced by calcining the dried powder at 400 °C for 2 h. The doped NiO (in weight ratio, NiO = $w(Ni(NO_3)_2.6H_2O)$ = 10, N/NiO = $w(CO(NH_2)_2)/w(Ni(NO_3)_2.6H_2O)$ = 1:9, Fe/NiO = $w(Fe(N\ O_3)0.9H_2O)/w\ (Ni(NO_3)_2. 6H_2O)$ = 1:9, N/Fe/NiO = $w(CO(NH_2)_2)/w\ (Fe(NO_3). 9H_2O)/w(Ni(NO_3)_2. 6H_2O)$ = 1:1:8, can be obtained. SDS increased the dissoluble of the ingredients in water while also catalysing the reaction significantly. SDS is also essential for preventing random aggregation in synthesised nanoparticles and assisting in the formation of unique morphologies.

2.3 Characterization techniques

SEM (JEOL-SEM) and TEM (TEM Philips CM 200) examine topography of synthesized products. XRD facilitates structural information in terms of the diffraction angle range of 30°–80° (PANalytical X'Pert). UV–Vis spectrometer (Ocean optics 4000) was used to investigate the

absorption-catalytic properties of synthesised materials. An X-ray photoelectron spectrometer (Kratos AXIS-HS) states chemical entity of prepared NiO composites. In order to investigate the luminescence properties, photo-luminescence spectra were recorded by fluoromax spectrofluorometer using a GaAs photomultiplier tube detector with the excitation wavelength, 351 nm (Horriba, HR2000, Fluorolog -3, Light Source−450 W Xenon Lamp: Wavelength Accuracy−0.5 nm, Detector: visible (200–800 nm)-PMT and NIR (800–1500 nm)). All measurements were performed at room temperature. The photocurrent treatments were executed in a photo-catalytic reactor. It is rectangular in shape and has a cooling water jacket. It's area, power, voltage, intensity equals to 26×41 cm^2, 150 W, 24 V and 11.9 W/m^2, respectively. Gas chromatography-mass spectroscopy was used to assess the by-products (GCMS-QP 2010 Plus Shimadzu mass spectrometer).

2.4 Photocatalysis

In an aqueous solution, the photocatalytic behaviour of synthesised products was tested using MB as a dye model. The photocatalyst was made up of four separate powders: NiO, N/NiO, Fe/NiO, and N/Fe/NiO. In a typical experiment, 30 mg of photo-catalyst was mixed in 100 ml of 3×10^{-5} M dye solution and agitated for 45 min to achieve equilibrium. The mixture was then irradiated. 5 mL of the mixture was taken out at regular intervals to be analyzed for knowing the dye concentration using a UV–Vis spectrophotometer.

The proportion of dye degradation (%) was estimated using Eq. 3 [25]:

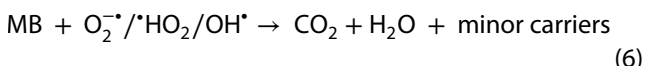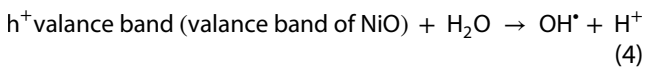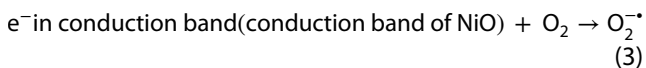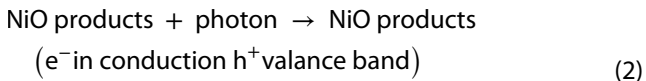$$\% = \frac{C_0 - C_t}{C_0} \times 100 \qquad (1)$$

where; C_0 and C_t are solution's absorbance values at 0 min and t min, respectively.

A photo-catalytic reaction is triggered when an absorbed photon has energy (hv) that is comparable to the band gap of the photo-catalyst NiO and its composites (Fig. 1). The energy absorbed on the NiO nanocomposites causes the generation of charge carriers (electron and proton) [Eq. (4)]. These photo-induced electrons (e) and holes (h +) combine with O_2 and H_2O, high-reactive super-oxide radicals ($^\bullet O_2^-$) (Eqs. (5) and hydroxyl radicals (OH$^\bullet$) [Eq. (6)] are produced. Superoxide radicals cause formation of hydroperoxy ($^\bullet HO_2$) radicals when it react with protons (H$^+$) [Eq. (7)]. All these radicals were then oxidized MB into CO_2 and H_2O [Eq. (8)]. However, because NiO has a lower adsorption capacity, it is not a good candidate for easy electron transit between the excited dye and irradiation, which restrain the dye from degrading, as illustrated in Fig. 1(I). N, on the other hand, has the ability to build high concentrations of excess charge, which aids the photocatalytic process by reducing e–h recombination in the NiO volume, allowing radical species to attack the R–S + = R functional group in MB, as shown in Fig. 1 (II). Additionally, the three-dimensional Fe nanoparticles could generate charge carrier density via the delayed photon effect, which improved light harvesting and hence resulted in better photocatalytic activity (Fig. 1 (III)). Furthermore, as shown in Fig. 1 (IV), the combination of N and Fe could

Fig. 1 Schematic illustration of the fabrication of nanoparticles (left), such as (i) NiO, (II) N/NiO, (III) Fe/NiO, and (IV) N/Fe/NiO and their usability in the photocatalytic process for the breakdown of MB
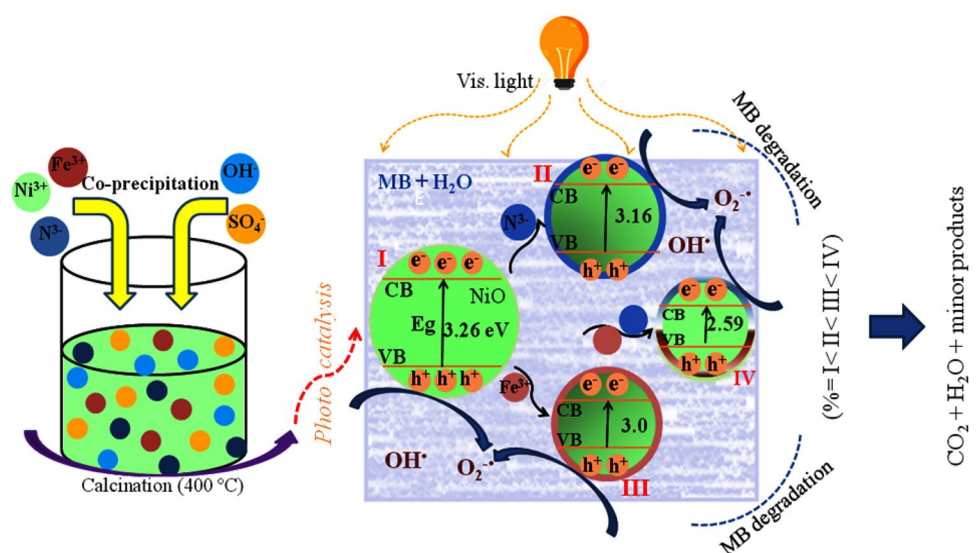
significantly boost the photocatalytic effectiveness of NiO by increasing the density of possible reaction sites, which could form more e^- h^+ couples.

$$NiO\ products\ +\ photon\ \rightarrow\ NiO\ products$$
$$\left(e^-\ in\ conduction\ h^+ valance\ band\right) \tag{2}$$

$$e^-\ in\ conduction\ band(conduction\ band\ of\ NiO)\ +\ O_2\ \rightarrow\ O_2^{-\bullet} \tag{3}$$

$$h^+ valance\ band\ (valance\ band\ of\ NiO)\ +\ H_2O\ \rightarrow\ OH^\bullet\ +\ H^+ \tag{4}$$

$$O_2^{-\bullet}\ +\ H^+\ \rightarrow\ ^\bullet HO_2 \tag{5}$$

$$MB\ +\ O_2^{-\bullet}/^\bullet HO_2/OH^\bullet\ \rightarrow\ CO_2 + H_2O\ +\ minor\ carriers \tag{6}$$

The hydroxyl radical rate during irradiation of samples was detected by fluorescence spectroscopy using terephthalic acid: 30 mg photocatalysts was mixed in 50 mL aqueous terephthalic acid solution (1 mM). The solution was agitated for 45 min in the dark and then exposed to irradiation with a tungsten halogen light (380–800 nm, 24 V/150 W). A part of the mixture was centrifuged to isolate the photo catalyst. Finally, the remaining solution's fluorescence was calculated by excitation at 315 nm.

3 Results and discussion

3.1 Structural properties of NiO nanoproducts (XRD & XPS)

The XRD pattern was reported and illustrated in Fig. 2a to analyse the crystallinity of the prepared products. The characteristic diffraction peaks in all the samples have been assigned to the FCC lattice of NiO [JCPDS Card No: 01-078-0423] with a lattice constant of 4.174. Figure 2a shows the diffraction peak shifting slightly higher angles with N/&Fe doping, in the order of $\theta_{NiO} < \theta_{N/NiO} < \theta_{Fe/NiO} < \theta_{N/Fe/NiO}$. Furthermore, the amplitude of all diffraction peaks was significantly reduced in the order of N/Fe/NiO < Fe/NiO < N/NiO < NiO. The crystallite size of these products has been detected from the following equation [26, 27].
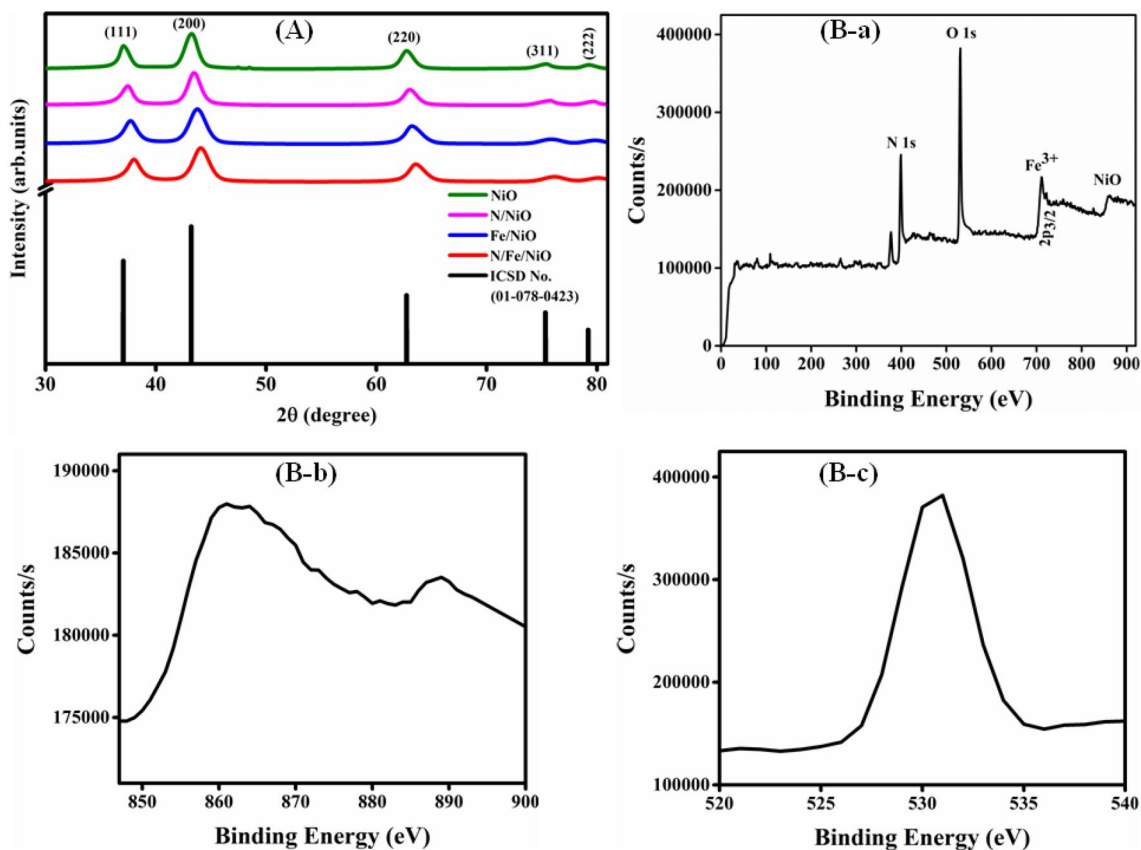
$$D = K\lambda/\beta cos\theta \tag{7}$$

Fig. 2 XRD spectra in **a** larger scale, and **b** smaller scale and **c** XPS of undoped NiO and doped NiO NPs

where K is a Scherer constant, D is the crystallite size, λ is X-ray wavelength (~ 0.54 Å), θ is the angle of diffraction and β is the FWHM. For NiO, N/NiO, Fe/NiO, and N/Fe/NiO, the grain sizes were determined to be 6.67 nm, 5.32 nm, 4.52 nm, and 3.76 nm, respectively. The grain size of Fe/NiO NPs and N/Fe/NiO NPs was lower than that of undoped NiO NPs and N/NiO NPs, which can be explained by the fact that Fe^{3+} and N^{3-} ions increase the nucleus number of NiO NPs when they incorporate. The dislocation density (δ) can also be detected using the following equation.

$$\delta = n/D^2 \tag{8}$$

Table 1 Structural and optical properties of undoped NiO and doped NiO NPs

Sample	Crystallite size (nm)	Dislocation density ($\times 10^{15}$ m^2)	Band gap (eV)
NiO	6.67	22.47	3.23
N/NiO	5.32	35.33	3.15
Fe/NiO	4.52	48.94	3.0
N/Fe/NiO	3.76	67.16	2.56

where "D" is mean grain size and n equal to 1. The results are given in Table 1.

The XPS spectra of undoped NiO nanoparticles are shown in Fig. 2bb-c. The two dissimilar peaks in Fig. B (b), centred at 886.4 eV and 860.1 eV, are assigned to Ni^{2+} ions in undoped NiO, due to $2P_{1/2}$ and $2P_{3/2}$ transitions, respectively. At 530 eV [28], the equivalent O 1 s peak of Ni oxide can be seen in Fig. B (c). Figure 2b a illustrates the XPS spectra of doped NiO nanoparticles by Fe and N [29]. Fe 2p3/2 is caused by the peak at 712.03 eV. Also, a peak about 404.3 eV corresponds to the typical N 1 s spectrum. As a result, the Fe and N dopants are presented in the experimental powders. The binding energies discovered are very similar to those described in the XPS manual [30].

3.2 Optical properties of NiO nanoproducts (UV–Visible & PL)

The optical properties of the synthesised NiO products are shown in Fig. 3. The absorption-wavelength spectrum of NiO products shows a characteristic absorption edge in the range 314–325 nm, which is due to electronic transitions between energy levels, as shown in Fig. 3a. It also referred that the absorption of doped NiO slightly
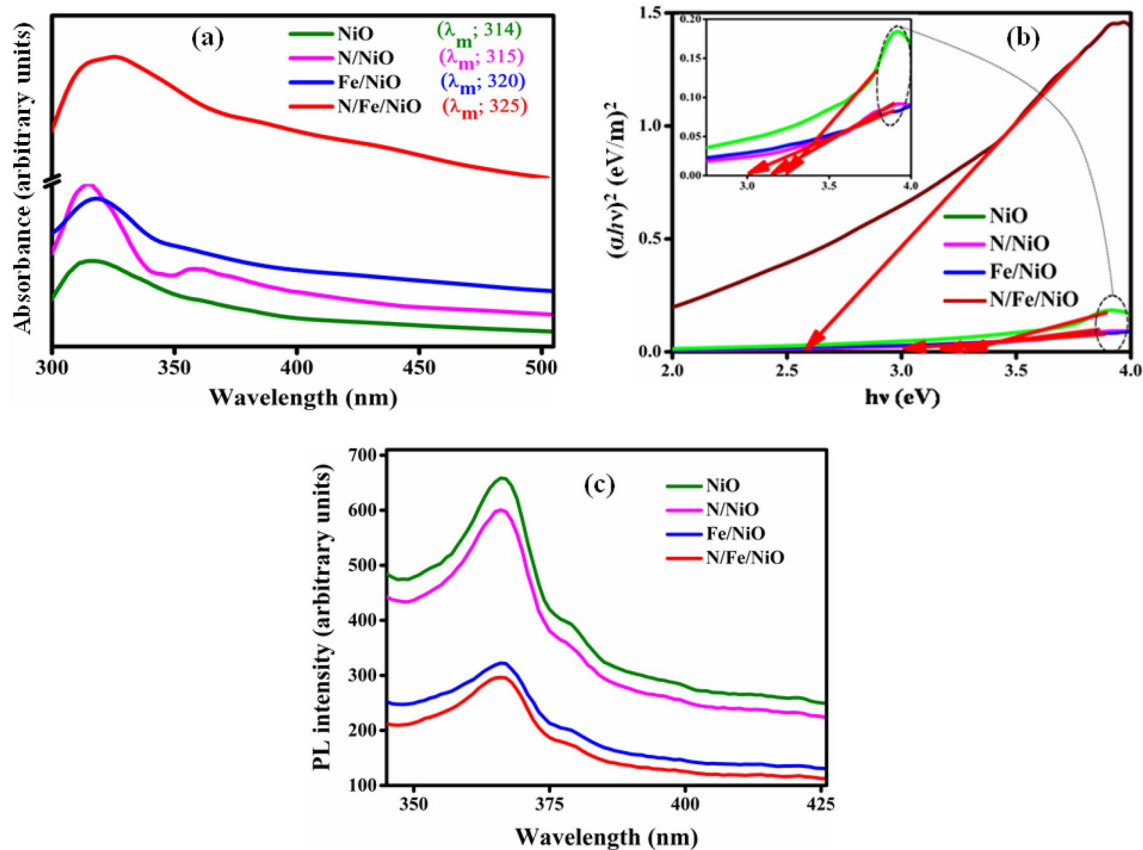

Fig. 3 **a** UV–visible absorption, **b** band gap and **c** PL spectrum of the undoped and doped NiO NPs

shifted towards the higher wavelength with respect to the pure NiO, which is attributed to the smaller crystallite size [31, 32]. Since the absorption coefficient's energy dependency indicates the presence of a direct band gap using Tauc's plot (Fig. 3b), and the band gap (Eg) is calculated by extrapolating the linear portion [33, 34]. The obtained direct band gap is 3.26, 3.16, 3.0 and 2.59 eV for the NiO, N/NiO, Fe/NiO and N/Fe/NiO, respectively, which shifted towards the lower energy with respect to the pure NiO due to the huge size distribution of synthesized materials and as confirmed by our SEM findings.

The PL curves from four separate NiO samples were illustrated in Fig. 3c. They show strong peak at 370 nm due to the radiative recombination of the charge carriers. The disparity in emission intensity is independent with size and morphology of the variations. As a result, we can see that NPs size decreased from 6.9 to 4.1 nm, the PL intensity decreased. By doping NiO nanocrystals with N and/or Fe ions, structural studies revealed that the NiO nanocrystals have additional defects such as cationic impurities and surface vacancies. Increases in cation vacancies and surface related defects, which act as alternative non-radiative pathways to PL emission, cause a decrease in PL strength for N and/ Fe-doped

nanocrystals, rather than the presence of oxygen vacancy related states [35, 36]. However, in the N doped nanocrystals, there are a few cation vacancies, resulting in a partial reduction in luminescence intensity.

3.3 Topographical properties of NiO nanoproducts (SEM, TEM etc.)

To elucidate the morphology of the prepared products, we performed SEM and TEM imaging on a series of samples (Figs. 4, 5). In Fig. 4, imaging of NiO showed that the surface morphology consisted a rock like shape that is produced by assembling various sized NiO nanoparticles (Fig. NiO), while the N/NiO microparticles possessing considerable layers of N on the surface of the NiO particles due to the evaluation of the large amount of gases during the addition of nitrogen ions onto the NiO lattice (Fig. N/NiO). By replaced with Fe, the Fe ions are incorporated into NiO lattice, which is clearly seen by the block coating on the surface of the Fe/NiO nanocrystals, in orderly (Fig. Fe/NiO), Fe and N nanoparticles assembled to form precipitates and block coating on the NiO nanoparticles by being joined one on another during the synthesis of N/Fe/NiO nanocomposite (Fig. N/Fe/NiO). It is noted that the brightness
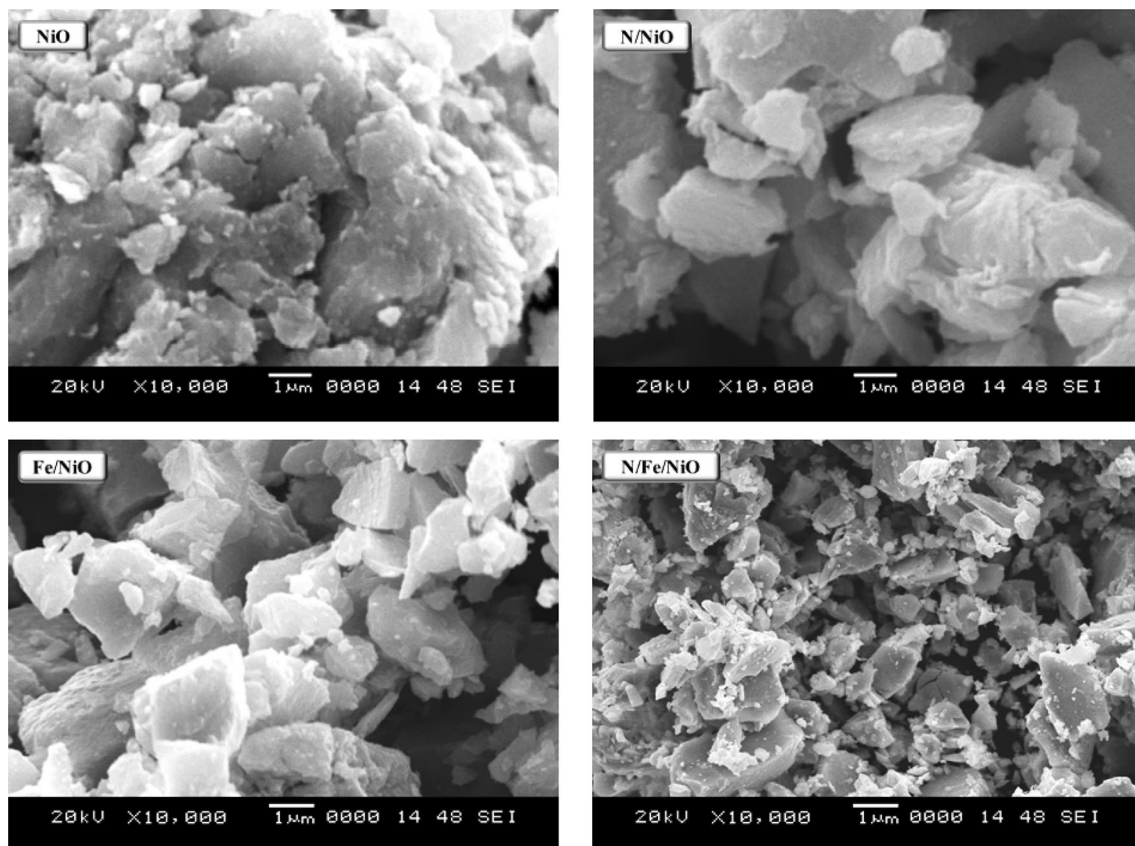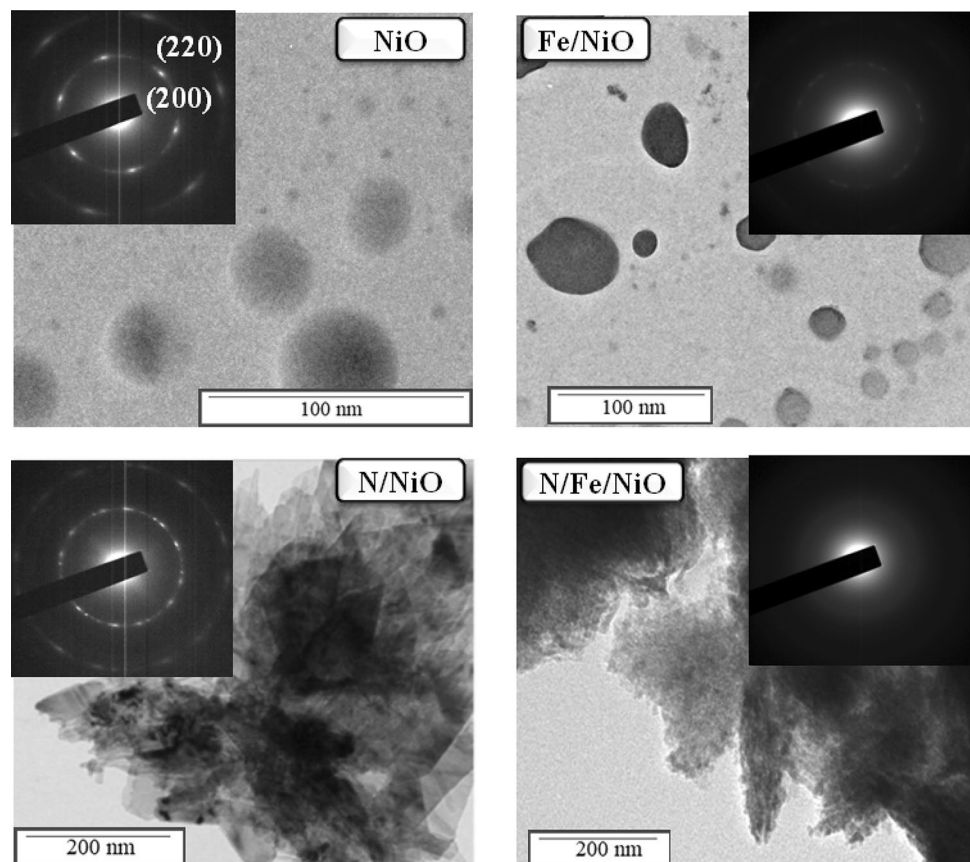

Fig. 4 SEM micrographs of the undoped and doped NiO NPs calcined at 400 °C

Fig. 5 TEM includes SEAD micrographs of the undoped NiO and doped NiO NPs calcined at 400 °C

of certain spots in the above figures (Fe/NiO and N/NiO) is due to a reduction in charging or a rise in voltage.

The topography of various synthesised NiO products were determined using TEM analysis. NiO and N/NiO particles have a size, ranging ~ 20 to 50 nm, while Fe/NiO and N/Fe/NiO have a size around 10–25 nm. The NiO and Fe/NiO particles were spherical in shape and well distributed with a flat surface and identical size, while the N/NiO and N/Fe/NiO nanoparticles aggregated into secondary particles (Fig. 5). The SAED pattern consists of two diffraction rings with different radii correspond to (200) and (220) planes, respectively (as shown in the inset of Fig. 5). SAED pattern of the NiO nanoparticles obtained by chemical precipitation confirmed the crystalline diffraction planes. Further it was well matched with XRD of NiO nanoproducts. The particle diameter specified by TEM appropriately matched with the mean grain size measured using the Scherer formula from the XRD patterns.

The elemental composition of Ni, O, Fe and N atoms in the respected samples was analyzed by EDS, as shown in Fig. 6. Since a greater amount of Ni precursor was used, Ni and O were classified as the major elements in the chemical composition of the synthesised compound. In addition to NiO, the associated composites contained large concentrations of Fe and small amounts of N. This indicates that Fe^{3+} and N^{3-} impurities have joined the NiO crystal matrix, replacing O^{2-} ions rather than occupying the interstitials [37].

4 Photocatalytical properties of NiO nanoproducts

Figure 7 shows optical properties of various catalysts based on UV–visible absorption spectra. The UV–visible spectrum of MB was characterized by two types of absorptions. One absorption at 283 nm associated to benzene with the $\pi \rightarrow \pi^*$ transition, while the other absorption at 664.3 nm corresponds to covalent bonded with the nitrogen group in the MB molecule. The dye amount was estimated by measuring the highest absorbance value at max = 596 nm from the spectra at reaction time ranging ~ 0–6 h. The intensity of the absorption edge decreases with reaction time, and the overall wavelength of absorption shifts dramatically towards lower wavelengths, suggesting catalytic decay of MB [38].
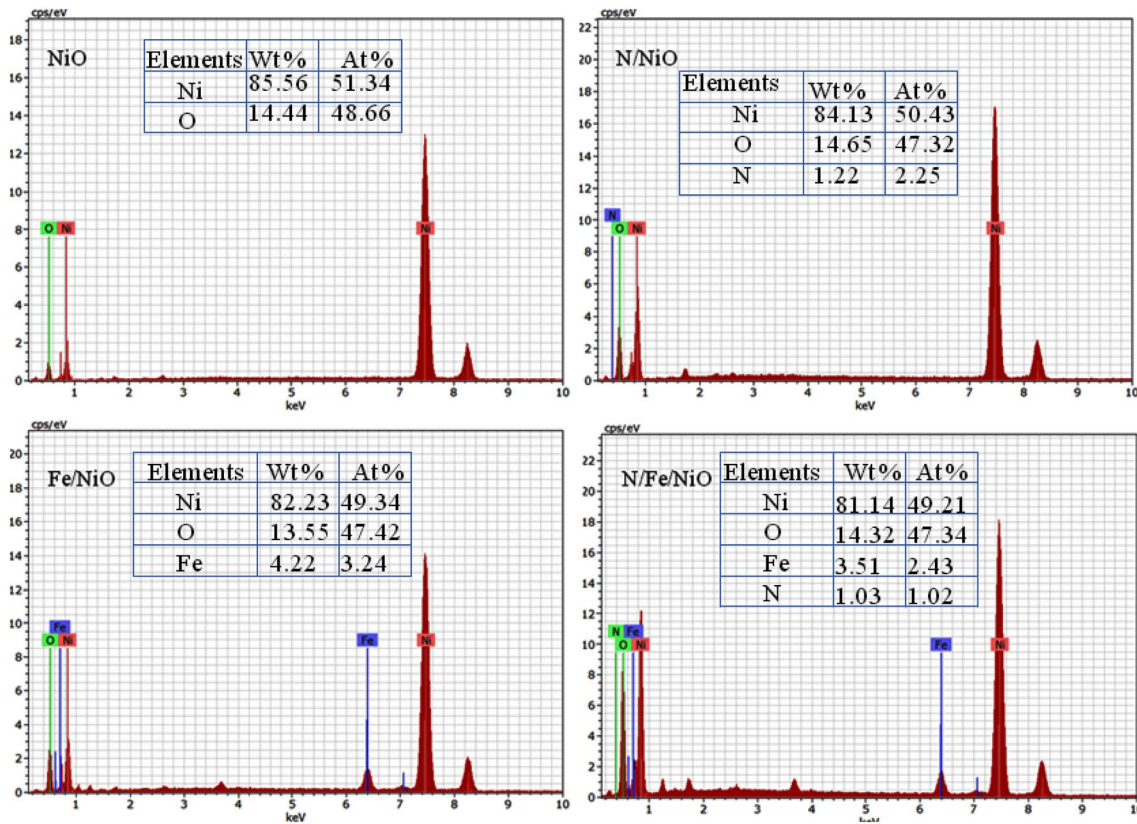
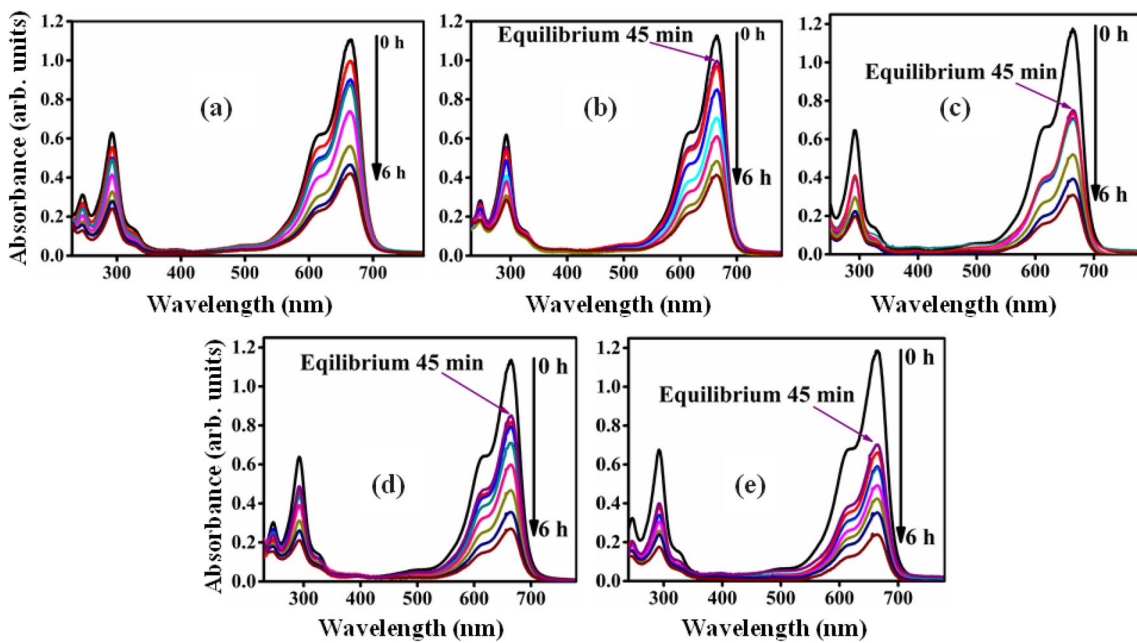**Fig. 6** EDAX images of the undoped NiO and doped NiO NPs calcined at 400 °C

Fig. 7 Absorption-wavelength spectra for the breakdown of MB dye (dye concentration = 9.59 mg/L, photo catalyst dose (NiO & its composites) = 0.3 g/L, pH = 7, light bulb dimensions = 24 V/150 W, reactor size = 26 × 41 cm^2, light intensity = 11.9 W/m^2, temperature = 30 °C and time = 6 h)

To know the effectiveness of catalyst blank test was performed: it was discovered that there was no difference in catalytic activity between the blank and pure NiO catalysts; however, the catalytic activity was increased after doping with N, Fe. This is due to the shrinking of the band gap, which allows light to pass from the UV to the Vis region. Since NiO cannot absorb visible light because its band gap is 3.26 eV. For N/Fe/NiO, Fe/NiO, N/NiO, NiO and even without a catalyst, the dye degradation efficiency is 79.8%, 76.3%, 73.8%, 62.8%, and 61.5% in 6 h, respectively (Fig. 8). As a result, it's worth noting that N/Fe/NiO as a photocatalyst resulted in a decolorization rate of 79.8 percent in just 6 h. The synergistic effect of Fe, N, and NiO, which efficiently facilitates the separation and transfer of charge carriers, accounts for the increased photocatalytic activity of N/Fe/NiO. Besides, nitrogen served as an electron trap from the CB of N/Fe/NiO, adsorbing O_2 to produce $\cdot O_2^-$. These photogenerated reactive radical species of $\cdot O_2^-$, $\cdot OH$, N^{3-}, Fe^{3+} worked together to efficiently degrade MB to H_2O and CO_2, resulting in increased photocatalytic activity [39, 40].

Figure 9b depicts the creation of fluorescent products in various nanocomposites, along with quantitative estimates. The presence of a fluorescent peak at 431 nm that progressively enhances in intensity with reaction time, suggesting accelerated hydroxyl radical creation, is shown in the results (Fig. 9a). However, under similar conditions, the amount of $OH^\cdot$ formation varies for different nanocomposite. The amount of hydroxyl radical could be expressed by the ratio of final intensity to initial intensity value (I/I_0) is detected at 431 nm. N/Fe/NiO, in particular, produces more hydroxyl radicals than NiO and its nanocomposites, and it produces the highest hydroxyl radical rate among the composites studied, including NiO, N/NiO, and Fe/NiO. These findings indicate that N/Fe/NiO will be the best photo catalyst of all the samples examined (Fig. 9a).

The breakdown yield produced at the end of the 6 h reaction was examined using GC–MS, and mass spectra data was used to recognise the N/Fe/NiO photocatalyst (Fig. 10a). The peaks at m/z ratios of 94, 109, 136, 158, 218.6, and 292, as shown in Fig. 10b, correspond to organic by-products quite well [41, 42].

4.1 Kinetics of NiO nanoproducts

The kinetics of photocatalytic degradation of MB by various photocatalysts are shown in Fig. 11 and can be represented using the equations below [43].

$$C_t - C_0 = -k_0 t \text{ (zero order)} \tag{9}$$

$$\ln\left(C_t/C_0\right) = -k_1 t \text{ (First order)} \tag{10}$$

$$1/C_t = k_2 t \text{ (second order)} \tag{11}$$

where C_0 is the dye concentration at 0 s and C_t is the dye concentration at t sec, and k is the rate constant.

Table 2 shows the measured rate constants (k) and corresponding R^2 values for the photo decomposition of MB by various catalysts. Zero, first, and second order kinetic models are used to test the experimental sorption data for
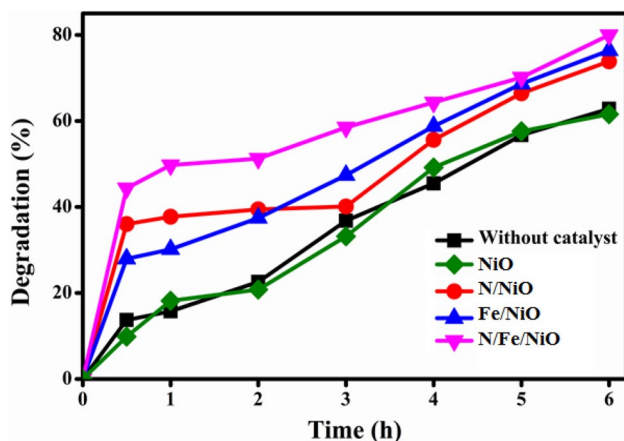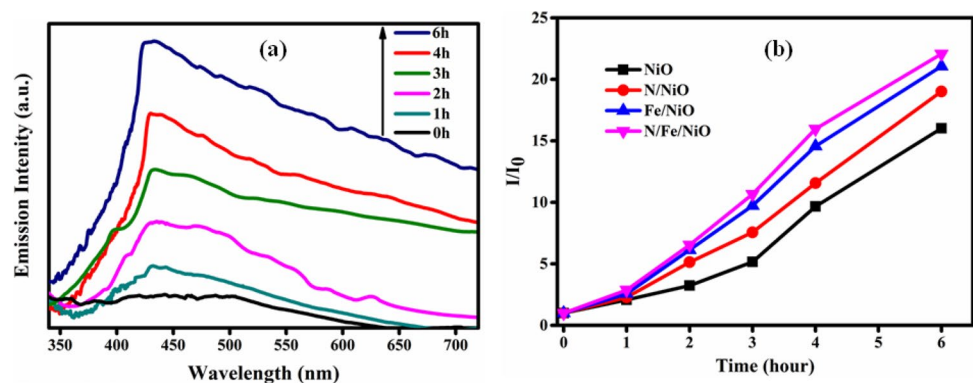
Fig. 8 Effect of reaction time on the MB degraded by various NiO products

Fig. 9 **a** fluorescence spectra for the different times during the irradiation of N/Fe/NiO with terephthalic acid (1 mM) in water (excitation, λexc = 315 nm; emission, λem = 431 nm), and **b** production rate of OH· by different photocatalyst under identical situations

Fig. 10 a Gas chromatography–mass spectrometry chromatograms obtained for decomposition of MB with the catalysts N/Fe/NiO observed after 6 h and **b** decomposition pathway proposed for MB degradation
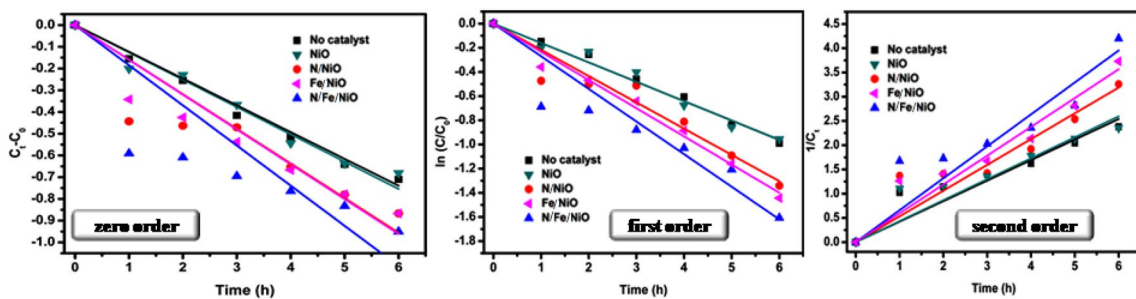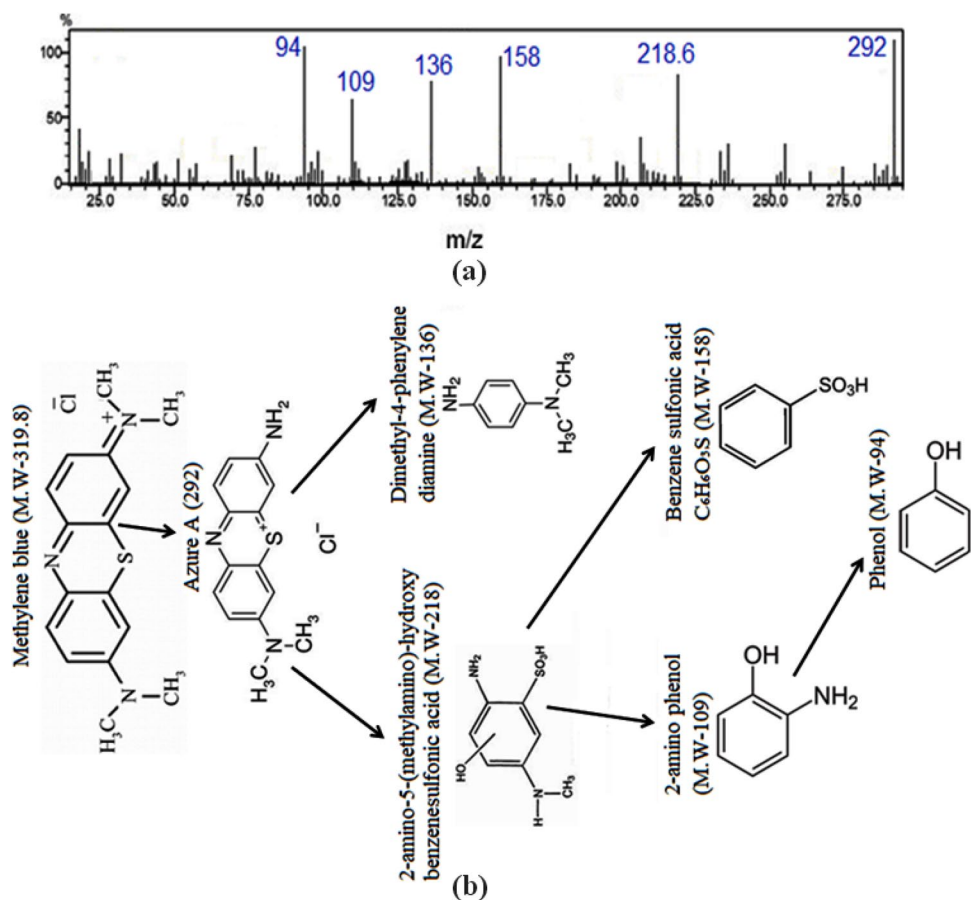

Fig. 11 Kinetic graphs for the MB onto various NiO products at the room temperatures

Table 2 Linear correlation coefficients (R^2), rate constant (k) of the zero order (mol $l^{-1} h^{-1}$), first order (h^{-1}) and second order (l mol h^{-1}) for photo-catalytic degradation of MB by different NiO NPs under visible light

Material	Zero-order kinetic		First –order kinetics		Second –order kinetics	
	K	R^2	k	R^2	k	R^2
No catalyst	−0.1847	0.90476	−0.27	0.96019	0.65	0.95
NiO	−0.1593	0.9740	−0.2332	0.9749	0.53	0.96
N/NiO	−0.1231	0.989	−0.2172	0.9902	0.43	0.96
Fe/NiO	−0.1601	0.9720	−0.1605	0.9945	0.59	0.97
N/Fe/NiO	−0.1256	0.99626	−0.1603	0.99597	0.42	0.96

MB-photocatalyst systems. For the MB-photocatalyst sorption, the R^2 value for the pseudo first order kinetic equation was detected to be higher than that of the pseudo zero order and pseudo second order kinetic equation. The rate of degradation of MB by NiO NPs is the following order: without catalyst≈NiO < N/NiO < Fe/NiO < N/Fe/NiO.

The enhanced catalytic activity of N/Fe/NiO NCs can be interpreted in terms of optical and structural properties. To begin, XRD results show that the mean crystal size of N/Fe/NiO is small, with higher dislocation density than NiO, which increases the quantum size effect due to the confinement of the electronic movement. This leads to the energy bands of the NiO change into discrete energy levels. As a consequence, the conduction band's electric potential changes more negative; otherwise, the valence band electric potential changes more positive. The oxidation–reduction potential of holes and electrons increased as a result, increasing the oxidation activity of NiO photocatalyst [44]. Charge recombination is also known to be a function of luminescence intensity. As shown in Fig. 3c, the PL intensity of N/Fe/NiO crystal was lower than NiO, N/NiO, and Fe/NiO, illustrating that the N/Fe/NiO nanoparticles efficiently segregated photo-generated charge carriers. As a result, it causes a lower charge carrier recombination rate, resulting in a dramatic synergistic effect on the photo efficiency of N/Fe/NiO NPs.

According to SEM studies, dopants are coated with NiO, which prevents NiO NPs from aggregating and serves as electron transfer channels for the generation of hydroxyl and peroxyl radicals, which have a high capability for the decomposition of MB. The thin N and Fe can also shorten the electron and ion diffusion paths, enhancing the photochemical catalyst's stability and rate capability. As a result, the N/Fe/NiO hybrid regarded as a potential catalyst for the decomposition of MB molecule and exhibit excellent catalytic properties [45, 46].

4.2 Recyclability of NiO nanoprducts

For three times, photocatalytic experiments were carried out utilising NiO, N/NiO, Fe/NiO, and N/Fe/NiO, as well as MB solutions. As demonstrated in Fig. 12, there was no significant change in the total concentration of the catalyst when exposed to visible light. NiO, N/NiO, Fe/NiO, and N/Fe/NiO photocatalysts retain over 96–99 percent of their original photocatalytic activity.

5 Conclusion

NiO nanocomposites were fabricated via a chemical precipitation route. The average crystal size of NiO products was determined from 6.67 to 3.76 nm using
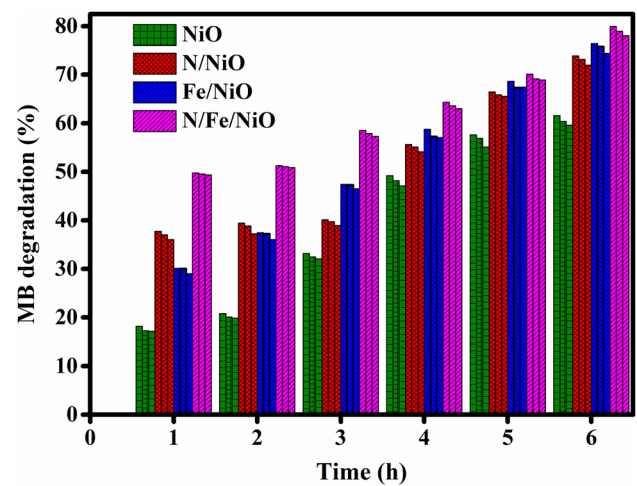
Fig. 12 Reusability data over various catalysts in the degradation of 100 ml of 3×10^{-5} M MB for different irradiation time under visible light

the Debye Scherrer formula based on XRD, whereas the mean particle diameter of NiO products was estimated to be in the range of 10–50 nm using TEM. The phase and morphology of NiO NPs alter when they are doped with iron, nitrogen, or both, ensuing in a decline in crystallite size and an increase in dislocation density, as assessed by XRD. In addition, the energy gap of composites was reduced from 3.2 to 2.5 eV, as estimated by Tauc Plots based on UV–visible analysis. The chemical state of the Fe and N doped NiO composites were also validated using XPS. This is remarkable since, when compared to undoped NiO, the N/Fe/NiO had a smaller crystallite size, higher dislocation density, and a lower band gap. These features boosted NiO's photocatalytic efficacy for the decomposition of MB; as a result, at 30 mg N/Fe/NiO irradiated with visible light for 6 h, up to 80% of MB was degraded. Besides, it is also advised that the fractal dimension, which is linked to a high density of porous structure and higher quantities of defects in N/Fe/NiO particles as estimated by photoluminescence, influences both MB adsorption and the creation of super oxide and hydroperoxy radical species. Also noteworthy is the fact that employing the precipitation method and nickel (II) nitrate as a precursor resulted in the development of a high number of oxygen vacancies, which played a key role in the production of hydroxyl radicals when visible radiation was used. According to these findings, the synthesized N/Fe/NiO may have a promising application for wastewater treatment when exposed to visible light irradiation.

Declarations

Conflict of interest The author declared no potential conflicts of interest with respect to the research, authorship, and/or publication of this article.

Human and animal rights This article does not contain any studies with human participants or animals performed by any of the authors.

Informed consent This article does not contain individual participants requiring informed consent.

References

1. Niu XZ (2019) Models to predict sunlight-induced photodegradation rates of contaminants in wastewater stabilisation ponds and clarifiers. Water Sci Eng 12(4):293

2. Alrazzak NA, Saad ST, Al-gubury HY, Kareem MM, Assi MM (2020) Photo catalytic degradation efficiency of azo dye in aqueous phase using different photo catalysts. Bull Chem Soc Ethiop 34(3):463

3. Thomas T, Kottam N (2013) Combining "chimie douce" and green principles for the developing world: improving industrial viability of photocatalytic water remediation. Chem Eng Sci 102:283

4. Goudarzi MG, Bagherzadeh M, Taheri F, Vartooni AR (2020) Preparation and characterization of magnetic zirconium oxide nanocomposite as a catalyst for reduction of methylene blue. SN Appl Sci 2:1249

5. Bielska M, Szymanowski J (2006) Removal of methylene blue from waste water using micellar enhanced ultrafiltration. Water Res 40(5):1027

6. Golder AK, Hridaya N, Samanta AN, Ray S (2005) Electrocoagulation of methylene blue and eosin yellowish using mild steel electrodes. J Hazard Mater 127(1):134

7. Makeswari M, Saraswathi P (2020) Photo catalytic degradation of methylene blue and methyl orange from aqueous solution using solar light onto chitosan bi-metal oxide composite. SN Appl Sci 2:336

8. Khairnar SD, Patil MR, Shrivastava VS (2018) Hydrothermally synthesized nano crystalline Nb_2O_5 and its visible-light photocatalytic activity for the degradation of Congo red and methylene blue. Iran J Catal 8(2):143–150

9. Patil MR, Khairnar SD, Shrivastava VS (2016) Synthesis, characterisation of polyaniline–Fe_3O_4 magnetic nanocomposite and its application for removal of an acid violet 19 dye. Appl Nanosci 6:495–502

10. Hudin N, Diantoro M, Kusumaatmaja A, Triyana K (2018) Study on photocatalytic properties of TiO_2 nanoparticle in various pH condition. J Phys 1011:012069

11. Warsi MF, Bilal M, Zulfiqar S, Khalid MU, Agboola PO, Shakir I (2020) Enhanced visible light driven photocatalytic activity of MnO_2 nanomaterials and their hybrid structure with carbon nanotubes. Mater Res Express 7:105015

12. Khairnar SD, Kulkarni AN, Shinde SG, Marathe SD, Marathe YV, Dhole SD, Shrivastava VS (2021) Synthesis and characterization of 2-D La-doped Bi_2O_3 for photocatalytic degradation of organic dye and pesticide. Photochem Photobiol 6:100031

13. Maniammal K, Madhu G, Biju V (2018) Nanostructured mesoporous NiO as an efficient photocatalyst for degradation of methylene blue: structure, properties and performance. Nano-Struct Nano-Objects 16:266

14. Khairnar SD, Shrivastava VS (2019) Facile synthesis of nickel oxide nanoparticles for the degradation of methylene blue and rhodamine B dye: a comparative study. J Taibah Univ Sci 13(1):1108–1118

15. Rokhsat E, Khayatian A (2018) Enhanced photocatalytic activity of fe doped ZnO hierarchical nanosheets on the degradation of p-nitrophenol under visible light. Inorg Nano-Met Chem 48(3):203

16. Hu S, Wang A, Li X, Löwe H (2010) Hydrothermal synthesis of well-dispersed ultrafine N-doped TiO2 nanoparticles with enhanced photocatalytic activity under visible light. J Phys Chem Solids 71(3):156

17. Davar F, Fereshteh Z, Salavati-Niasari M (2009) Nanoparticles Ni and NiO: synthesis, characterization and magnetic properties. J Alloys Compd 476(1–2):797

18. Li Q, Wang L-S, Hu B-Y, Yang C, Zhou L, Zhang L (2007) Preparation and characterization of NiO nanoparticles through calcination of malate gel. Mater Lett 61(8–9):1615

19. Xin X, Lü Z, Zhou B, Huang X, Zhu R, Sha X, Zhang Y, Su W (2007) Effect of synthesis conditions on the performance of weakly agglomerated nanocrystalline NiO. J Alloys Compd 427(1–2):251

20. Ma M-G, Zhu J-F, Jiang J-X, Sun R-C (2009) Hydrothermal–polyol route to synthesis of β-Ni (OH) 2 and NiO in mixed solvents of 1, 4-butanediol and water. Mater Lett 63(21):1791

21. Qiao H, Wei Z, Yang H, Zhu L, Yan X (2009) Preparation and characterization of NiO nanoparticles by anodic arc plasma method. J. Nanomater 2009:1–5

22. Aslani A, Oroojpour V, Fallahi M (2011) Sonochemical synthesis, size controlling and gas sensing properties of NiO nanoparticles. Appl Surf Sci 257(9):4056

23. Anandan K, Rajendran V (2012) Structural, optical and magnetic properties of well-dispersed NiO nanoparticles synthesized by CTAB assisted solvothermal process. Nanosci Nanotechnol Int J 2(4):24

24. Ahmad T, Ramanujachary KV, Lofland SE, Ganguli AK (2006) Magnetic and electrochemical properties of nickel oxide nanoparticles obtained by the reverse-micellar route. Solid State Sci 8(5):425

25. Sahoo C, Gupta AK, Pillai IMS (2012) Photocatalytic degradation of methylene blue dye from aqueous solution using silver ion-doped TiO_2 and its application to the degradation of real textile wastewater. J Environ Sci Health Part A 47(10):1428

26. Cheong KY, Muti N, Ramanan SR (2002) Electrical and optical studies of ZnO: Ga thin films fabricated via the sol–gel technique. Thin Solid Films 410(1):142

27. Williamson GK, Smallman RE (1956) III. Dislocation densities in some annealed and cold-worked metals from measurements on the X-ray debye-scherrer spectrum. Philos Mag 1(1):34

28. Hanifehpoura Y, Morsalib A, Mirtamizdoustc B, Jooa SW, Soltani B (2017) Thermolysis synthesis of pure phase NiO from novel sonochemical synthesized Ni (II) nano metal-organic supramolecular architecture. Ultrason Sonochemistry 37:430–435

29. Salavati-Niasari M, Mohandes F, Davar F, Mazaheri M, Monemzadeh M, Yavarinia N (2009) Preparation of NiO nanoparticles from metal-organic frameworks via a solid-state decomposition route. Inorg Chim Acta 362(10):3691

30. Moura KO, Lima RJS, Coelho AA, Souza-Junior EA, Duque JGS, Meneses CT (2014) Tuning the surface anisotropy in Fe-doped NiO nanoparticles. Nanoscale 6(1):352

31. El-Kemary M, Nagy N, El-Mehasseb I (2013) Nickel oxide nanoparticles: synthesis and spectral studies of interactions with glucose. Mater Sci Semicond Process 16(6):1747

32. Kumar PV, Ahamed AJ, Karthikeyan M (2019) Synthesis and characterization of NiO nanoparticles by chemical as well as green routes and their comparisons with respect to cytotoxic effect and toxicity studies in microbial and MCF-7 cancer cell models. SN Appl Sci 1:1083

33. Beydoun D, Amal R, Low G, McEvoy S (1999) Role of nanoparticles in photocatalysis. J Nanoparticle Res 1(4):439

34. Tauc J (1968) Optical properties and electronic structure of amorphous Ge and Si. Mater Res Bull 3(1):37

35. Gandhi AC, Wu SY (2017) Strong deep-level-emission photoluminescence in NiO nanoparticles. Nanomaterials 7(8):231

36. Sarkar A, Khan GG (2019) The formation and detection techniques of oxygen vacancies in titanium oxide-based nanostructures. Nanoscale 11(8):3414

37. Naik GDL, Kottam N, Shivashankar GK (2010) Photo catalytic degradation of azo dyes over Mn^{2+} doped TiO_2 catalyst under UV/solar light: an insight to the route of electron transfer in the mixed phase of anatase and rutile. Chin J Chem 28(11):2151

38. Das S, Bandi V, Arora HS, Veligatla M, Garrison S, D'Souza F, Mukherjee S (2015) Synergistic catalytic effect of iron metallic glass particles in direct blue dye degradation. J Mater Res 30(08):1121

39. Mahanthappa M, Kottam N, Yellappa S (2019) Enhanced photocatalytic degradation of methylene blue dye using CuSCdS nanocomposite under visible light irradiation. Appl Surf Sci 475:828

40. Huang S, Xu Y, Xie M, Xu H, He M, Xia J, Huang L, Li H (2015) Synthesis of magnetic CoFe2O4/g-C3N4 composite and its enhancement of photocatalytic ability under visible-light. Coll Surf Physicochem Eng Asp 478:71

41. Gnaser H, Savina MR, Calaway WF, Tripa CE, Veryovkin IV, Pellin MJ (2005) Photocatalytic degradation of methylene blue on nanocrystalline TiO2: surface mass spectrometry of reaction intermediates. Int J Mass Spectrom 245(1–3):61

42. Xia S, Zhang L, Pan G, Qian P, Ni Z (2015) Photocatalytic degradation of methylene blue with a nanocomposite system: synthesis, photocatalysis and degradation pathways. Phys Chem Chem Phys 17(7):5345

43. Khairnar SD, Shirsath DS, Patil PS, Shrivastava VS (2020) Adsorptive and photocatalytic removal of carcinogenic methylene blue dye by SnO2 nanorods: an equilibrium, kinetic and thermodynamics exploration. SN Appl Sci 2:822

44. Colmenares JC, Luque R, Campelo JM, Colmenares F, Karpiński Z, Romero AA (2009) Nanostructured photocatalysts and their applications in the photocatalytic transformation of lignocellulosic biomass: an overview. Materials 2(4):2228

45. Li G, Lv L, Fan H, Ma J, Li Y, Wan Y, Zhao XS (2010) Effect of the agglomeration of TiO_2 nanoparticles on their photocatalytic performance in the aqueous phase. J Coll Interface Sci 348(2):342

46. Wojcieszak D, Kaczmarek D, Domaradzki J, Mazur M (2013) Correlation of photocatalysis and photoluminescence effect in relation to the surface properties of TiO2: Tb thin films. Int J Photoenergy 2013:1–9